

Multiscale investigation of the structure and morphology of the Co/Fe₂O₃(0001) interfaceO. Bezencenet,^{1,*} H. Magnan,¹ C. Mocuta,² E. Fonda,² S. Stanescu,² P. Ohresser,² R. Belkhou,² and A. Barbier^{1,†}¹CEA, IRAMIS, SPCSI, F-91191 Gif-sur-Yvette Cedex, France²Synchrotron SOLEIL, L'Orme des Merisiers, Saint-Aubin, F-91192 Gif-sur-Yvette Cedex, France

(Received 22 December 2009; published 17 February 2010)

We report a detailed structural characterization of Co films grown on α -Fe₂O₃(0001) for thicknesses up to 25 nm. Epitaxial and single-crystalline 20 nm thick α -Fe₂O₃(0001) layers deposited on α -Al₂O₃(0001) and Pt(111) single crystals were used as substrate. The Co/ α -Fe₂O₃(0001) interface is a prototypical magnetic exchange coupled system for which the magnetocrystalline parameters are crucial to address. We evidence medium range order requiring a multiscale approach to reach a reliable description of the crystalline structure. Surface extended x-ray absorption fine structure (EXAFS) and surface x-ray diffraction (SXRD) have been combined to describe the structure in an extended thickness range. Additional grazing incidence small angle x-ray scattering (GISAXS) measurements show that the growth is three dimensional up to \sim 3 nm and follows a nucleation—growth—coalescence scheme. For all thicknesses cobalt is found to grow with a lattice parameter close to its bulk lattice parameter. In the early stages of growth a disordered 2–3 monolayer thick interface exhibiting oxidized cobalt and metallic iron is evidenced. Long range order sets in for thickness above 4 nm showing the coexistence of fcc, twinned fcc, and hcp stacking within direct and in-surface-plane 30° rotated epitaxial relationships.

DOI: 10.1103/PhysRevB.81.085419

PACS number(s): 61.05.cj, 61.05.cf, 68.55.–a, 75.70.–i

I. INTRODUCTION

Magnetically exchange coupled ferromagnetic (FM)/antiferromagnetic (AF) interfaces have important practical and industrial applications and have attracted much attention since the discovery of the phenomenon 50 years ago by Meiklejohn and Bean.¹ They are of great interest for a broad range of applications in the field of modern spintronics.² The magnetic exchange coupling manifests itself through two possible effects: an exchange bias field H_E corresponding to a hysteresis loop shift along the field axis and, a possible enhancement of the coercive field, H_C .^{3,4} The correlation of the FM and AF domain structures was shown for Co/LaFeO₃(001),⁵ Co/NiO(001),⁶ and Co/ α -Fe₂O₃(0001) (Ref. 7) bilayers. The presence of interfacial uncompensated AF spins, has been proposed as being a key feature of the FM/AF magnetic exchange coupling.

Despite active research and numerous reported models^{8–11} the exchange-bias effect is still subject to controversies. Many studies evidence the importance of the interface structure¹² and in particular the AF domains structure near the interface.^{12–16} A detailed characterization of the crystalline structure at the interface is a mandatory step in order to understand the magnetic exchange coupling for a given system. Unfortunately a number of epitaxial films and interfaces are far from ideal and cannot be easily investigated because no unique technique enables a reliable characterization.

In the present work, we explore the structure of Co/ α -Fe₂O₃(0001)/ α -Al₂O₃(0001) and Co/ α -Fe₂O₃(0001)/Pt(111). In a previous study we have demonstrated that the FM Co and AF hematite magnetic domains are coupled.⁷ Hematite (α -Fe₂O₃), the most stable iron oxide, is a promising antiferromagnetic material^{17–19} for applications, since its Néel temperature (955 K) is significantly higher than room temperature (RT). It is a very common material in Earth crust and is thus highly stable, environment

friendly and cheap. Hematite films thicker than 3 nm deposited by atomic oxygen assisted molecular beam epitaxy either on Pt(111)²⁰ or α -Al₂O₃(0001) (Ref. 21) substrates mimic almost all properties of bulk hematite except the Morin transition.²⁰ Co is a ferromagnetic three-dimensional (3D) transition metal with a high-Curie temperature (1388 K). The Co/hematite interface may be considered as one of the model systems for the study of AF/FM coupling with a low-AF in-plane anisotropy. It is also a medium crystalline ordered interface that cannot be described easily with a single experimental technique.

The paper is organized as follows. We first describe the sample elaboration and the experimental techniques. Then we present the long range ordering using surface x-ray diffraction (SXRD) (Sec. III A). Next the short range ordering in the early stages of growth is investigated using surface extended x-ray absorption fine structure (SEXAFS) (Sec. III B) and finally the morphology of the films is questioned by grazing incidence small angle x-ray scattering (GISAXS) investigations (Sec. III C). Concluding remarks are given in Sec. IV.

II. EXPERIMENTAL

The hematite layers, of thickness 20 nm, were grown in a dedicated setup^{22,23} by atomic oxygen assisted molecular beam epitaxy on α -Al₂O₃(0001) or Pt(111) substrates as described in Ref. 24. The structure and the stoichiometry of the iron oxide films were systematically checked *in situ* by reflection high-energy electron diffraction (RHEED) and x-ray photoelectron spectroscopy (XPS). Bulk hematite crystallizes in the hexagonal corundum structure (space group $R\bar{3}c$) with six formula units and with following lattice parameters: $a=b=5.038$ Å and $c=13.772$ Å.²⁵ For both substrates, α -Al₂O₃(0001) and Pt(111), the epitaxial α -Fe₂O₃ layers

crystallize in the rhombohedral crystal structure ($R\bar{3}c$ space group) with parameters very close to the expected bulk values [$a=5.033\pm 0.05$ Å and $c=13.88\pm 0.2$ Å when deposited on α -Al₂O₃(0001) and $a=5.05\pm 0.05$ Å and $c=13.5\pm 0.3$ Å when deposited on Pt(111)].²⁴ The surface plane has a hexagonal symmetry and the nearest neighbor distance between iron (respectively, oxygen) is 5.033 Å (respectively, 2.905 Å). The overall properties of the hematite films are similar on both substrates with following differences: Pt(111) substrates lead to better crystallized layers (mosaic spread $\sim 0.45^\circ$ compared to 2.3° for Al₂O₃ substrates), which include the presence of an ordered dislocation network²⁴ at the interface and the presence of a 50% twinning of the layers, i.e., two lattices with a 30° in-surface-plane relative orientation grow simultaneously.²⁴ The surface EXAFS, SXRD, and GISAXS measurements required air exposure of the samples; after introduction in a new ultrahigh vacuum (UHV) vessel an annealing during 30 min at a sample temperature of ~ 600 K under a 10^{-5} mbar oxygen partial pressure²⁴ proved to regenerate successfully the surface without any phase changes. The typical α -Fe₂O₃(0001) surface roughness was ~ 1 Å r.m.s. as deduced from specular reflectivity estimations. The roughness is slightly larger when using α -Al₂O₃(0001) substrates as can be deduced from reflection high-energy electron diffraction patterns that show less strikes.

The surface EXAFS experiments were carried out at the synchrotron SOLEIL (France), on the SAMBA beamline, using a Si(111) double crystal monochromator at the Co K -edge (7710 eV). The EXAFS spectra are recorded in the fluorescence yield mode. The SXRD and GISAXS measurements were performed on the ID01 (anomalous diffraction) beamline at the European Synchrotron Radiation Facility (ESRF, Grenoble, France). A vertical UHV setup²⁶ (base pressure 1×10^{-10} mbar), holding a horizontal sample surface, with a 360° 1 mm thick Be window equipped with a furnace, an ion gun, an oxygen gas line and an Omicron™ EFM3 evaporation cell were installed on a 2+2 diffractometer. The monochromatic beam of wavelength $\lambda=0.688$ Å (i.e., photon energy 18 keV) was vertically and horizontally focused down to a size of 150×220 μm^2 [full width at half maximum (FWHM)]. The presample slits (located at about 1 m upstream the sample) were set to 250×350 μm^2 and 250×50 μm^2 (V \times H) for SXRD and GISAXS measurements, respectively. The limiting slits prior the detector (avalanche photodiode located at ~ 61 m from the source and 1 m from the sample) were typically set to 4×0.1 mm² (respectively, 4×1 mm²) for GISAXS (respectively, SXRD) in surface plane measurements and 0.4×0.2 mm² (respectively, 1×4 mm²) for GISAXS (respectively, SXRD) out of surface plane measurements. Bulk hematite lattice parameters were used to index the reciprocal space during the SXRD experiment: $a=b=5.038$ Å and $c=13.772$ Å.²⁵

On both setups, a high-purity Co rod (grade 99.999%) was electron bombarded (typical emission current 25 mA under an electric potential of 750 V) to deposit the thin films (typical evaporation rate 2 Å/min) on the sample held at RT. The film thickness (t_{Co}) was calibrated by a quartz microbal-

ance and refined in the SRXD setup using specular reflectivity scans ($\theta/2\theta$), which are highly sensitive to the deposited layer thickness. All the measurements were carried out at RT.

III. RESULTS AND DISCUSSION

A. Long range order and thick layers: SXRD

For the SXRD studies Pt(111) single crystalline substrates were used since they promote the best ordered α -Fe₂O₃(0001) films. Because of the intrinsically large lattice mismatch of Co(0001) versus α -Fe₂O₃(0001), a pseudomorphic epitaxy cannot be expected here. The RHEED patterns recorded during growth (not shown) are quite fuzzy with broad spots that are roughly compatible with a $(\sqrt{3}\times\sqrt{3})R30^\circ$ epitaxial relationship, but this technique alone can neither provide a precise determination of the structure nor determine the lattice parameters of the epitaxial layer.

SXRD offers high-surface sensitivity tunable through the glancing incidence angle geometry and large penetration depths due to the short hard x-ray wavelengths. It is thus an ideal technique to investigate the crystalline structure of an epitaxial layer for thicknesses ranging from the submonolayer regime up to tens of nanometers thick layers. In-surface-plane scans were recorded during the growth with the incidence and emergence angles close to the critical angle for total external reflection of the x-rays. It is common practice to approximate the small resulting out of plane L value by 0 (although it would precisely be 0.05 in reciprocal lattice units (r.l.u.) of α -Fe₂O₃(0001)). The in-surface-plane scans performed along the high-symmetry directions ($[hh0]$ and $[0k0]$) are reported in Fig. 1. Up to $t_{Co}\leq 0.4$ nm no changes in reciprocal space could be observed. Above $t_{Co}=0.4$ nm broad features appear at $(\sim 1.2; \sim 1.2; 0)$ and $(0; \sim 2.1; 0)$. These peaks correspond to Co(010) and Co(010) $R30^\circ$ reflections, respectively, where $R30^\circ$ indicates a lattice in plane rotated by 30° . The scattered intensities of the Co(010) and Co(010) $R30^\circ$ are similar; it is likely that both lattices appear in equivalent quantities. These peaks develop to a complex shape, which resembles the initial shape of the (110) or (220) Bragg peaks of α -Fe₂O₃(0001) [Fig. 1(a)]. The satellite peaks originate from the scattering of the interfacial α -Fe₂O₃(0001)/Pt(111) coincidence lattice.²⁴ The shape of the Co(010) peaks show that the coincidence lattice network propagates into the Co overlayer. Because of this complex shape these peaks are hardly of any help to deduce the Co lattice parameters. The higher order Co Bragg peaks [Co(110), Co(020)...] have better defined shapes and allow extracting the in-surface-plane parameters (a_{Co}) reported in Table I.

Out-of-surface plane crystal truncation rods (CTRs)²⁷ were recorded. The α -Fe₂O₃(0001) (11L), (22L), and (30L) CTRs showed no interferences into the scattered signal and appeared insensitive to the Co growth even for very thick layers. This observation indicates that the Co atoms or any possible interface compound do not occupy the α -Fe₂O₃(0001) atomic sites. The Co (10L) $R30^\circ$ [Fig. 2(a)] and Co (11L) $R30^\circ$ [Fig. 2(b)] CTRs show epitaxial Co features for thickness above 1.6 nm. Along (11L) $R30^\circ$ fcc,

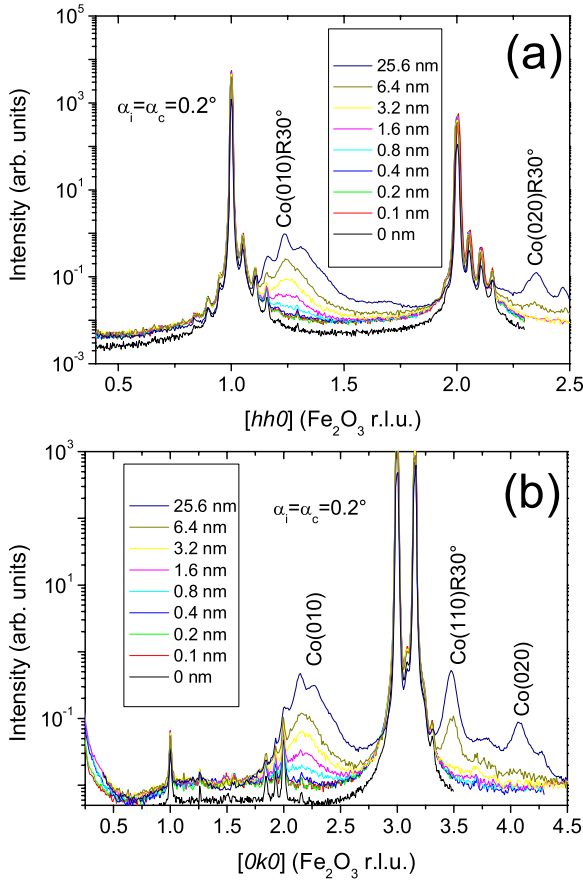


FIG. 1. (Color online) SXR D in surface plane scans recorded on Co/ α -Fe₂O₃/Pt(111) samples along the (a) $[hh0]$ and (b) $[0k0]$ reciprocal space directions with respect to the Co thickness: from bottom to top 0, 0.1, 0.2, 0.4, 0.8, 1.6, 3.2, 6.4, and 25.6 nm. The horizontal axes are labeled in α -Fe₂O₃ reciprocal lattice units (r.l.u.). The (110), (220), and (300) peaks are Bragg reflections from the hematite layer and the (3.3,0,0) peak is a Pt(111) Bragg peak. The satellite structures around (110) and (220) originates from an interfacial well ordered coincidence lattice as described in Ref. 24.

twinned fcc, and hcp stacking have common Bragg peaks (at $L \sim 0$ and $L \sim 7$ r.l.u.) whereas each stacking produce an individual and well separated peak along $(10L)R30^\circ$. We see that as soon as the long range order is sufficient to produce SXR D scattering all 3 types of stacking appear in quantitatively the same proportion. From the L positions of the peaks

TABLE I. Lattice parameters (a_{Co} and c_{Co}) and peak widths (FWHM) [$\Delta_{Co(010)R30}$ and $\Delta_{Co(110)R30}$] derived from in and out-of-surface-plane SXR D scans.

t_{Co} (nm)	a_{Co} (Å)	c_{Co} (Å)	$\Delta_{Co(010)R30}$ (°)	$\Delta_{Co(110)R30}$ (°)
1.6	2.51	4.07	10 ± 1	
3.2	2.51	4.07	13 ± 1	12 ± 1
6.4	2.51	4.07	15 ± 1	12 ± 1
12.8	2.51	4.07	16 ± 1	11 ± 1
25.4	2.51	4.07	22 ± 2	12 ± 1

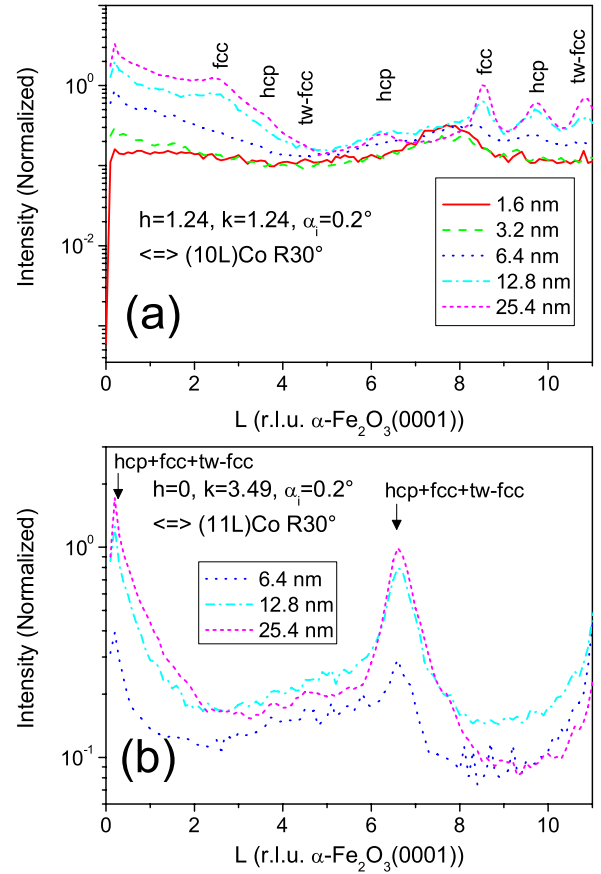


FIG. 2. (Color online) SXR D out of surface plane scans (crystal truncation rods of Co) recorded on Co/ α -Fe₂O₃/Pt(111) samples along the (a) $[10L]_{Co}$ and (b) $[11L]_{Co}$ reciprocal space directions with respect to the Co thickness.

we deduce the out of plane lattice parameters (c_{Co}) reported in Table I.

For all thicknesses for which we could extract the lattice parameters (Table I) we obtain parameters close to bulk Co; the layers are, thus, fully relaxed. The in-surface-plane Co Bragg peaks were found to exhibit Lorentzian type shapes; we have included in Table I the FWHM values of the Co(010) $R30^\circ$ and Co(110) $R30^\circ$ Bragg peaks [$\Delta_{Co(010)R30}$ and $\Delta_{Co(110)R30}$]. They are fairly large and dominated by a mosaic spread of about 10–12° for $t_{Co} \leq 3.2$ nm. Above this thickness we found a mosaic spread of 6° and a small coherent domain size of 0.8 nm.

The SXR D study shows that the Co layer is relaxed but fairly disordered. It remains an epitaxial layer (0001) oriented but with all possible types of stacking: fcc, twinned fcc, and hcp. It also include an additional in-surface-plane twinning since a 30° disoriented lattice grow along with the direct lattice. The lack of signal in the early stages of growth originates from (i) the intensity expected for a given Co Bragg peak is split between 3 [(110) like peaks] or 6 (any other peaks) twin peaks and from (ii) the intrinsically large mosaic spread (several degrees). SXR D is here hardly of any help to describe the Co structure for $t_{Co} \leq 1$ nm.

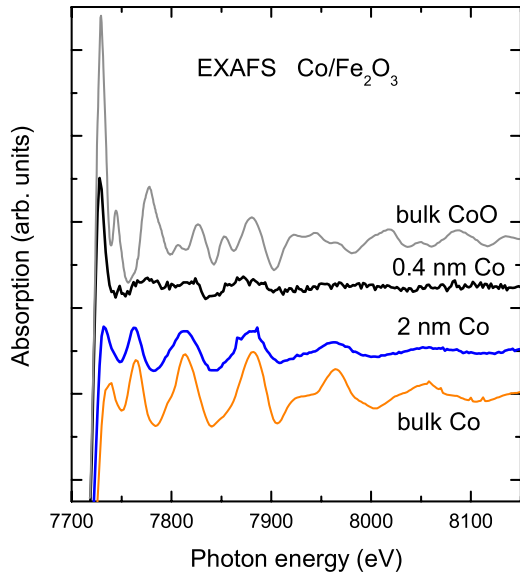


FIG. 3. (Color online) EXAFS spectra recorded at 300K at the Co *K*-edge for 0.4 and 2 nm of Co deposited on Fe₂O₃/Al₂O₃(0001) in grazing incidence, compared with spectra of bulk Co and bulk CoO

B. Early stages of growth and short range order: surface EXAFS

For the surface EXAFS studies α -Al₂O₃(0001) single crystalline substrates were mainly used. Surface EXAFS is well suited in order to determine the crystallographic structure of thin films even if they only exhibit medium range ordering.²⁸ It is a chemically selective method: by measuring the EXAFS oscillations above the *K*-edge of cobalt we are only sensitive to the local order in the entire cobalt film. Taking advantage of the linear polarization of the synchrotron radiation, EXAFS allows us to measure the nearest neighbor distances around Co atoms in all crystallographic directions with the same accuracy.^{29,30} We have studied 0.4 to 2 nm thick cobalt layers by surface EXAFS. For each sample, we have recorded two spectra, with the x-rays coming in normal incidence (polarization of the x-rays parallel to the surface plane) or in grazing incidence (polarization almost perpendicular to the surface plane). For all samples, (from 0.4 to 2 nm) no difference between normal and grazing incidences could be observed, this observation allows us to conclude that the structure of the cobalt film is isotropic. The raw EXAFS spectra recorded on 0.4 and 2 nm are presented in Fig. 3, together with the spectra obtained on bulk Co and bulk CoO.

The overall shape of the EXAFS oscillations is different for the 0.4 and 2 nm films: the spectrum of the 2 nm thick film looks like the bulk Co one and the spectrum of the 0.4 nm thick deposit has a pronounced oxidized cobalt contribution. The presence of oxidized cobalt at low coverage is consistent with the shapes of the XPS and x-ray absorption near-edge structure (XANES) spectra (Fig. 4). The shape of the XANES spectrum and the position of the white line for 0.4 nm are consistent with a mixing between metallic Co and CoO. We can exclude a contribution of Co₃O₄ since this

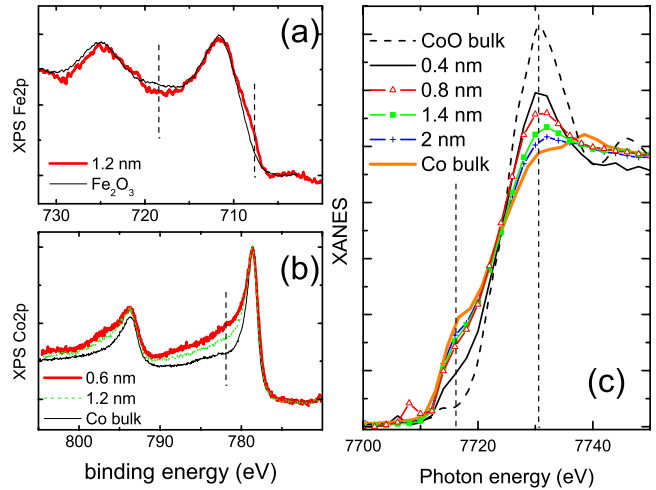


FIG. 4. (Color online) (a) XPS Fe 2p for Fe₂O₃ film and for 1.2 nm Co/Fe₂O₃, (b) XPS Co 2p for Co bulk, 0.6 and 1.2 nm Co/Fe₂O₃/Al₂O₃(0001) taken at a photon energy $h\nu=1253.6$ eV, (c) XANES spectra at the Co *K*-edge for CoO, 0.4, 0.8, 1.4, and 2 nm Co/ α -Fe₂O₃/ α -Al₂O₃(0001) and bulk Co. Dashed lines indicate the position of (a) metallic Fe 2p_{3/2} and Fe³⁺ satellite, (b) Co²⁺ satellite and (c) 7716.5 and 7730.5 eV photon energy

latter oxide shows a white line in the absorption spectrum at higher energy.³¹ The amount of metallic and oxidized Co can be evaluated from the XANES spectra by measuring the relative intensities of the structures at 7716.5 and 7730.5 eV. The intensities of these structures vary linearly with the cobalt thickness, and assuming that the oxidized cobalt is in the CoO oxidation state, we can evaluate the thickness of the oxidized cobalt. Above 0.4 nm, this thickness is found constant with increasing Co film thickness and amounts about 1.5 ML (monolayer) equivalent cobalt (0.3 nm). Co 2*p* XPS spectra confirm also the presence of oxidized cobalt at low coverage (see the structure at 782 eV binding energy³²).

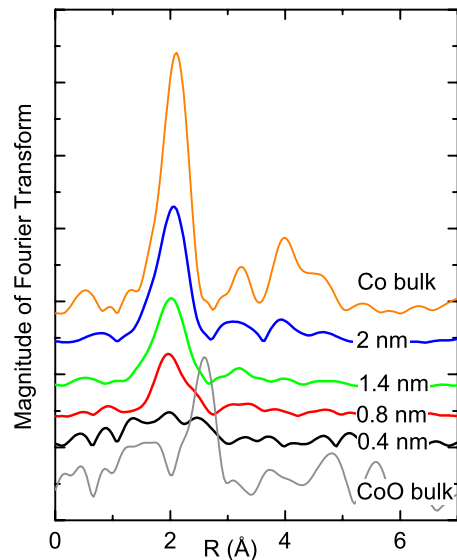


FIG. 5. (Color online) FT (from $k=2.51$ to 12.7 \AA^{-1} of $k\chi(k)$) for 0.4, 0.8, 1.4 nm and 2 nm in grazing incidence Co/ α -Fe₂O₃/ α -Al₂O₃(0001), Co bulk and CoO bulk.

TABLE II. Structural parameters for the first NN determined by least-squares fits of experimental data recorded in normal incidence at 300 K for Co/Fe₂O₃/Al₂O₃(0001) films, for Au/2 nm Co/Fe₂O₃/Pt(111) film (2*), compared with the values determined for a Co and CoO bulk crystals. N_i is number of effective number, R_i the mean NN distance around Co atoms and σ_i^2 is the mean square relative displacement around R_i , t^* is the equivalent thickness of the disordered cobalt given in monolayers (ML) with 1 ML=0.2 nm (see text).

t_{Co} (nm)	Co-Co pair			Co-Co pair			Co-O pair			t^* (ML)
	N_1	R_1 (Å) ±0.02	σ_1^2 (10 ⁻³ Å ²) ±1	N_2	R_2 (Å) ±0.03	σ_2^2 (10 ⁻³ Å ²) ±1	N_3	R_3 (Å) ±0.04	σ_3^2 (10 ⁻³ Å ²) ±1	
0.4	3.1	2.48	6	5.3	2.98	25	1.7	2.19	8	1.3
0.8	4.2	2.46	6.6	7.1	3.04	59				2.5
1.4	6.7	2.47	7.6	5	3.04	92				3
2	8.9	2.48	6	3	2.98	50				2.5
2*	10	2.49	4.7	2	2.98	22				1.7
Co bulk	12	2.50	2.3							
CoO bulk				12	2.98	5	6	2.12	8	

Moreover the Fe 2p XPS spectrum reveals that the film of α -Fe₂O₃ is also modified: we observe a decrease in the Fe³⁺ satellite at 718 eV binding energy,²³ and an increase of the metallic Fe structure at 708 eV binding energy after deposition of cobalt. This interfacial reactivity (reduction of hematite, occurrence of metallic iron and oxidized cobalt) has already been observed for Co/Fe₂O₃/Pt(111) samples.³³

A quantitative analysis of EXAFS spectra can be obtained by calculating the EXAFS oscillations using the classical procedure described in Ref. 28. A Fourier transform (FT) of the EXAFS oscillations (see Fig. 5) gives a series of peaks corresponding to the different shells of neighbors of the Co emitter atom; the main peak is due to the first nearest-neighbor (NN) shell and the peaks located at higher distances are due to more distant shells. One observes that the intensities of these peaks are very low as compared to references showing that the structure of the cobalt film is disordered. The inverse FT of the first peak allows to isolate the contribution of first NN from the total EXAFS signal. This contribution can be then fitted using the EXAFS formula in the single scattering approximation.²⁸ Amplitude and phase function for Co-Co pair are determined from a bulk Co reference EXAFS Spectrum, and for Co-O pair they have been calculated from FEFF³⁴ and checked on the experimental CoO EXAFS spectrum. The results of fits obtained for normal incidence spectra are summarized in Table II. The values for the NN distance and Debye Waller factor (σ^2) for the grazing incidence are the same as for the normal incidence for all thicknesses, so they are not reported in Table II.

We first discuss the results for films with thickness larger than 0.4 nm. For thicknesses above 0.4 nm the fits are performed fixing the number of total nearest neighbors to the theoretical value expected for a layer by layer growth mode assuming a hcp structure. Indeed, the presence of clusters on the surface with diameter larger than 2 nm (Ref. 33 and Sec. III C) will not change significantly the number of total nearest neighbors. Two shells of cobalt are necessary to fit the data: one shell with NN distance slightly below 2.5 Å (the value in bulk cobalt) and the second one around 3 Å (around the value of Co-Co distance in CoO). The Debye-Waller factor (σ^2) indicated in Table II includes static and thermal dis-

order. The first shell shows σ^2 values about two times larger than in bulk crystals, although the second shell shows σ^2 values thirty times larger than for reference. This second shell is then very disordered and due to the corresponding damping of the oscillations, its contribution to the total EXAFS signal is very small. The films of 1.4 and 2 nm have also been covered by 2 nm of Au at room temperature. For both films we observe no change of the crystallographic structure. The film of 2 nm cobalt deposited on α -Fe₂O₃/Pt(111) (2* in Table II) is fitted with 12 NN and shows however lower values of σ^2 and higher NN in the first shell as compared with the film deposited on Al₂O₃. This result will be discussed later.

The fit for the 0.4 nm spectra is performed with a free number of neighbors and the best fit gives 8.4 Co neighbors. This number is smaller than for a layer by layer growth (11.2 NN in normal incidence) and corresponds to the number of NN in spherical cluster with 1.2 nm diameter.³⁵ Moreover, for the 0.4 nm deposit it is also necessary to include a shell with oxygen neighbors, that is situated at a distance of 2.19 ± 0.04 Å which is close to the Co-O distance in cobalt oxides. The number of oxygen neighbors (1.7 NN) appears to be lower than expected for 1.5 equivalent monolayer of CoO (4.5 NN) estimated with XANES spectra. This can be due to the window used for the Fourier transform (from 2.5 to 11.6 Å⁻¹), this window is not adapted to oxygen neighbors, which have their contribution mainly below 3 Å⁻¹.

We can then conclude that the film of cobalt is made of a small amount of oxidized cobalt (around 1.5 equivalent monolayer of cobalt) and metallic cobalt. It is likely that, at room temperature, kinetic limitations hinder further diffusion which would be thermodynamically more favorable as already discussed in Ref. 33.

The metallic cobalt is simulated by two shells, a first shell is relatively ordered with NN distance around 2.5 Å as in bulk cobalt, and a very disordered second shell with larger NN distance; the number of Co neighbors in the disordered shell is large and it cannot be attributed to the 1.5 ML oxidized Co only. When the cobalt film thickness increases the proportion of cobalt situated in the ordered shell increases also. It is also the case when cobalt is deposited on

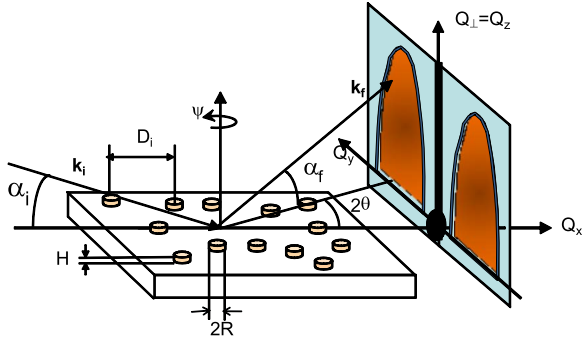


FIG. 6. (Color online) Geometry of the GISAXS experiment and angles description of the scattered \mathbf{k}_f and incident \mathbf{k}_i wave vectors yielding the momentum transfer (i.e., the reciprocal space vector) $\mathbf{Q}=\mathbf{k}_f-\mathbf{k}_i$. The angles α_i , α_f and $2\theta_f$ are related to the components of the momentum transfer, either parallel (Q_x and Q_y , with $Q_{\parallel}^2=Q_x^2+Q_y^2$) or perpendicular (Q_z or Q_{\perp}) to the sample surface. D is the interisland distance and R and H the radius and the height of islands.

α -Fe₂O₃/Pt(111). One may ask where the disordered cobalt is located? Since its amount is decreasing with thickness, we think that it is located at the interface. Within this hypothesis the equivalent thickness of disordered cobalt (t^*) is reported in the last column of Table II; one observes that above 0.4 nm, t^* is almost constant with thickness and amounts about 2.5–3 ML (1 ML=0.2 nm). At 0.4 nm the film consists of an assembly of clusters. Consequently, the surface is then not completely covered by cobalt, which can explain the lower t^* observed for this thickness. Moreover, we observe that t^* for the film deposited on platinum is slightly lower (1.7 ML). This can be related with lower rugosity of the hematite surface observed by RHEED, and higher crystalline quality observed by x-ray diffraction.²⁴ To conclude this section concerning the RT structure of Co/ α -Fe₂O₃ films of low thickness, we have shown that the interface of about 2–3 ML has a disordered structure including about 1.5 ML of oxide and that the structure above exhibits a better crystalline order with a lattice parameter close to the one of bulk cobalt.

C. Morphology: GISAXS

The typical geometry of a GISAXS experiment has been described in the literature^{36–41} and is recalled with our conventions in Fig. 6. The incident beam impinges the sample under an incidence angle α_i . The scattering signal from the islands near the forward direction is collected by a one or two-dimensional detector. The sample can be rotated around its surface normal by a Ψ rotation, which defines the orientation of the incident x-ray beam with respect to the in-plane crystallographic directions. In the present case, the Co islands show isotropic patterns with respect to a rotation around the surface normal. To the contrary, the residual signal originating from the dislocation network located at the α -Fe₂O₃(0001)/Pt(111) interface is only visible when incoming beam runs along the [010] crystalline direction of α -Fe₂O₃ (with sixfold symmetry), i.e., in azimuthal directions parallel to the network (signal located at $Q_{\parallel}=\pm 0.133 \text{ \AA}^{-1}$ in Fig. 7). The signal scattered from the

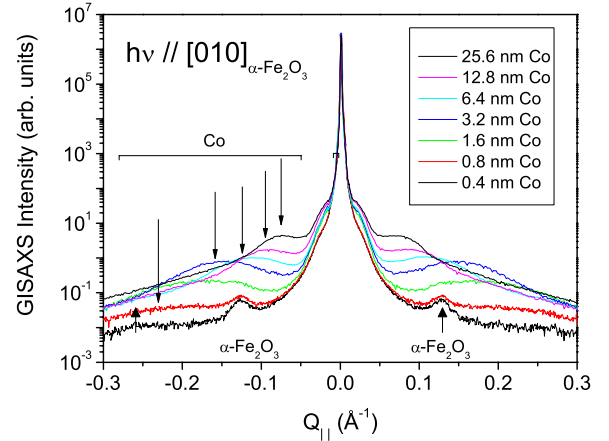


FIG. 7. (Color online) In-surface-plane GISAXS scans performed on Co/ α -Fe₂O₃/Pt(111) films in critical hematite incidence and emergence conditions ($\alpha_i=\alpha_f$) for increasing Co coverage (from bottom to top). The signal located at $Q_{\parallel}=\pm 0.133 \text{ \AA}^{-1}$ belongs to the interface dislocation network located at the Pt(111)/ α -Fe₂O₃ interface. It is best evidenced when the incoming beam runs along the [010] crystalline direction of α -Fe₂O₃ and has sixfold symmetry. The signal corresponding to the growing Co islands moves progressively toward $Q_{\parallel}=0$ and is isotropic with respect to the sample azimuth.

deposited Co layer is made of two lobes that moves toward the specular beam position ($Q_{\parallel}=0$) and sharpen with increasing Co thickness. Such a behavior is expected from an island nucleation-growth-coalescence process. The position of the maxima of the lobes in reciprocal space depends on the interisland distance and on the island form factor. From these positions one can only extract an approximate value of the interisland distances (D' in Table III). We will now describe a detailed analysis including the simulation of the experimental GISAXS scans, which is required to derive more precise values as well as additional morphological parameters.

In order to calculate the intensity scattered from the isotropic Co islands assembly, the incident beam is described by the wave vector $\mathbf{k}_i=k_0[\cos(\alpha_i), 0, -\sin(\alpha_i)]$, with the wavelength $\lambda=2\pi/k_0$, and the scattered wave by $\mathbf{k}_f=k_0[\cos(\alpha_f)\cdot\cos(2\theta_f), \cos(\alpha_f)\cdot\sin(2\theta_f), \sin(\alpha_f)]$ of equal modulus (k_0) where α_f and θ_f are the out-of-surface-

TABLE III. Morphology parameters derived from the best fit GISAXS scans with respect to the Co thickness, t_{Co} . The parameters indicated in bold are the most reliable, i.e., a significative change in shape of the calculated curves is obtained for a 1% variation of the value. D' is obtained from the maxima positions in Fig. 7.

t_{Co} (nm)	D (nm)	D' (nm)	R (nm)	σ_R	H (nm)	σ_H	ρ
0.4	2.2		1.6	$10 \cdot R$	0.55	$0.4 \cdot H$	0.3
1.6	3.0	3.6	2.6	$10 \cdot R$	1.4	$0.2 \cdot H$	0.3
3.2	3.5	4.2	2.7	$10 \cdot R$	2.05	$0.5 \cdot H$	0.3
6.4	4.6	5.4	2.7	$10 \cdot R$	2.7	$0.25 \cdot H$	0.3
12.8	6.8	6.6	2.7	$10 \cdot R$	6.5	$0.25 \cdot H$	0.3

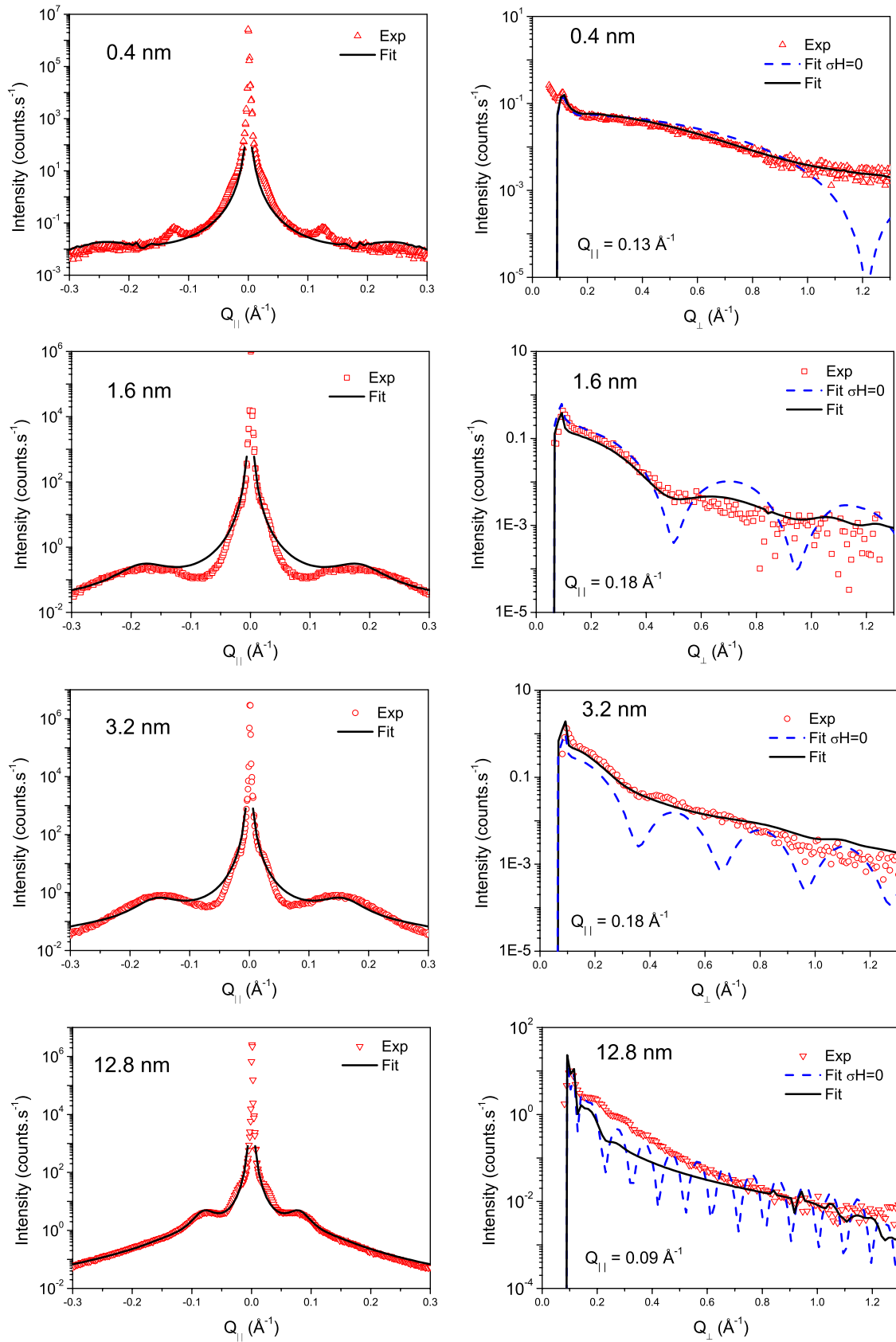


FIG. 8. (Color online) Experimental (symbols) and calculated (straight lines), in (left) and out (right) of surface plane GISAXS scans taken for $t_{Co}=0.4, 1.6, 3.2$ and 12.8 nm, at the $Q_{||}$ and Q_{\perp} values indicated in the graphs. The parameters of the fit are indicated in Table III. Dashed line is calculation assuming $\sigma_H=0$.

plane and in-surface-plane emergence angles respectively (Fig. 6). The momentum transfer or scattering vector \mathbf{Q} (that means the reciprocal space vector) is then given by $\mathbf{Q}=\mathbf{k}_f-\mathbf{k}_i$. It is convenient to decompose the momentum transfer into in-surface-plane (\mathbf{Q}_{\parallel}) and out-of-surface-plane (\mathbf{Q}_{\perp}) components. The distorted wave Born approximation (DWBA) formalism³⁶ was used to calculate the scattered intensities. It applies in geometrical conditions (incident or emergent) close to the total external reflection of x-rays, on very smooth surfaces, i.e., when the surface reflectivity is high, which is the case in our experimental conditions. In this approach the sample is considered as an assembly of islands and the substrate reflection has to be taken into account. We found that the Co islands were reasonably approximated to cylinders of height H and radius R ; thus, defining the form factor analytical expression

$$F_{cyl}(\mathbf{Q}, R, H) = 2\pi R^2 H \frac{J_1(Q_{\parallel}R)}{Q_{\parallel}R} \sin c\left(Q_z \frac{H}{2}\right) e^{iQ_z(H/2)},$$

$$\sin c(x) = \frac{\sin(x)}{x}. \quad (1)$$

Within the DWBA framework, the effective form factor $F(\mathbf{Q}_{\parallel}, k_i^z, k_f^z)$ is composed of four contributions, including all combinations of scattering from the islands and reflection from the substrate surface.³⁶ The effective form factor corresponds to the coherent interference of four waves corresponding to the four possible scattering events (weighted by the corresponding Fresnel incident and/or emergent reflection coefficients) experienced by the incoming and exiting beams on a given island.³⁶ The reflectivity coefficients were calculated within the recursive layer-by-layer Parratt formalism^{42,43} for the complete Co/ α -Fe₂O₃/Pt structure with following best fit parameters: α -Fe₂O₃ thickness 20 nm, α -Fe₂O₃ surface roughness 1 nm r.m.s., Pt surface roughness 0.2 nm r.m.s., Co surface roughness 1.5 nm r.m.s. The refraction indexes for x-rays of the elements involved in the sample, were taken from reference tables⁴⁴ for the experimentally used wavelength.

A paracrystal interference function $S(\mathbf{Q})$ for a Gaussian probability distribution has been used to take into account the positional disorder of the islands. For a Gaussian width ω and a characteristic interisland distance D one can write,

$$S(Q) = \frac{1 - e^{-(Q\omega)^2}}{1 + e^{-(Q\omega)^2} - 2e^{-(Q\omega)^2/2} \cos(QD)} \quad (2)$$

The ratio $\rho=\omega/D$ is a measure of the disorder in the paracrystal lattice and is linked to the widths of the interference function peaks. Including a broad paracrystal interference function was unable alone to describe the experimental scans. Additional log-normal distributions of H and R with widths σ_H and σ_R , respectively had to be introduced and the total signal results then from a double summation over the height and radius distributions leading to highly time consuming calculations for large σ_H and σ_R values.

Several cross-sections (Fig. 8), which are significant for the scattering process at different Q_{\parallel} and Q_{\perp} , were measured and simulated. This allows the determination and retrieval of

structural and morphological parameters (Table III). The experimental signal depletions close to the specular peak for the in-surface-plane scans for $t_{Co}=1.6$ nm and $t_{Co}=3.2$ nm are better reproduced for increasing σ_R values but to the cost of diverging calculation times. We have limited the calculations to $\sigma_R \leq 10 \cdot R$ that already stands for a very large distribution. The out-of-surface plane signal expected for $\sigma_H=0$ (i.e., no height distribution) has been included in Fig. 8—right (dashed line). It illustrates well the necessity to introduce such distributions to reasonably reproduce our data.

The parameters used to reproduce our experimental data are reported in Table III. For all thicknesses we reach the maximum value of $\sigma_R=10 \cdot R$ that we allowed. The σ_H values are less important but still quite large as well as the ρ values. The widths of the distributions show that the islands experience a very large dispersion in size and relative position. With increasing t_{Co} the interisland distances, the radii and heights increase, indicating a nucleation—growth—coalescence process. It is likely that the coalescence is correlated with the constant R value observed for $t_{Co} \geq 3.2$ nm; this observation is consistent with previous near field imaging and x-ray absorption observations^{33,45} that estimated the coalescence at $t_{Co} \sim 2$ nm.

As a conclusion, our GISAXS study shows that cobalt adopts a 3D growth on α -Fe₂O₃ within a typical nucleation—growth—coalescence scheme. However the large values of the width of distributions show that the size and the interdistance of islands are not well defined. Therefore, near field imaging techniques may hardly be of any help to characterize the average morphology of these layers since they will only produce a local view of a highly disordered and dispersed system.

IV. CONCLUSION

We have investigated the structure and morphology of Co layers deposited on α -Fe₂O₃ as a function of the Co thickness with complementary techniques. We find that cobalt grows within a nucleation—growth—coalescence scheme with a lattice parameter close to its bulk lattice parameter but with a 2—3 ML thick disordered interface including Co oxide and metallic iron. The combination of SXR, SEXAFS, and GISAXS appears as an interesting and complementary approach to fully describe the structure and morphology of medium ordered layers from the very early stages of their growth. This study will be helpful for the understanding of magnetic properties and magnetic coupling in this system.⁷ Particularly, we can clearly exclude a coupling due to a strong intermixing and/or an increase of the coercive field due to a particular crystallographic structure.

ACKNOWLEDGMENTS

We acknowledge the European Synchrotron Radiation Facility and Synchrotron SOLEIL for provision of synchrotron radiation facilities and we would like to thank the ID01 (ESRF), ID03 (ESRF), and SAMBA (SOLEIL) beamline staffs for providing excellent measurement conditions and assistance during measurements.

- *Present address: THALES Research and Technology France, 1 Avenue Augustin Fresnel, Campus de Polytechnique, F-91767 Palaiseau Cedex, France.
- †abarbier@cea.fr; <http://iramis.cea.fr/en/>
- ¹W. H. Meiklejohn and C. P. Bean, *Phys. Rev.* **102**, 1413 (1956).
 - ²S. S. P. Parkin, X. Jiang, C. Kaiser, A. Panchula, K. Roche, and M. G. Samant, *Proc. IEEE* **91**, 661 (2003).
 - ³M. D. Stiles and R. D. McMichael, *Phys. Rev. B* **63**, 064405 (2001).
 - ⁴C. Mocuta, A. Barbier, S. Lafaye, P. Bayle-Guillemaud, and M. Panabiere, *Phys. Rev. B* **68**, 014416 (2003).
 - ⁵F. Nolting *et al.*, *Nature (London)* **405**, 767 (2000).
 - ⁶H. Ohldag, A. Scholl, F. Nolting, S. Anders, F. U. Hillebrecht, and J. Stöhr, *Phys. Rev. Lett.* **86**, 2878 (2001).
 - ⁷O. Bezencenet, A. Barbier, P. Ohresser, R. Belkhou, S. Stanesco, H. Magnan, J. M. Tonnerre, S. Grenier, and M. J. Guittet, *J. Phys.: Conf. Ser.* **100**, 072027 (2008).
 - ⁸A. P. Malozemoff, *J. Appl. Phys.* **63**, 3874 (1988).
 - ⁹K. Takano, R. H. Kodama, A. E. Berkowitz, W. Cao, and G. Thomas, *Phys. Rev. Lett.* **79**, 1130 (1997).
 - ¹⁰D. Mauri, H. C. Siegmann, P. S. Bagus, and E. Kay, *J. Appl. Phys.* **62**, 3047 (1987).
 - ¹¹N. C. Koon, *Phys. Rev. Lett.* **78**, 4865 (1997).
 - ¹²J. Nogues and I. K. Schuller, *J. Magn. Magn. Mater.* **192**, 203 (1999).
 - ¹³C. Binek, X. He, and S. Polisetty, *Phys. Rev. B* **72**, 054408 (2005).
 - ¹⁴M. Fecioru-Morariu, J. Wrona, C. Papusoi, and G. Guntherodt, *Phys. Rev. B* **77**, 054441 (2008).
 - ¹⁵S. Urazhdin and C. L. Chien, *Phys. Rev. B* **71**, 220410(R) (2005).
 - ¹⁶J. Olamit and K. Liu, *J. Appl. Phys.* **101**, 09E508 (2007).
 - ¹⁷C. G. Shull, W. A. Strauser, and E. O. Wollan, *Phys. Rev.* **83**, 333 (1951).
 - ¹⁸R. Nathans, S. J. Pickart, H. A. Alperin, and P. J. Brown, *Phys. Rev.* **136**, A1641 (1964).
 - ¹⁹P. Kuiper, B. G. Searle, P. Rudolf, L. H. Tjeng, and C. T. Chen, *Phys. Rev. Lett.* **70**, 1549 (1993).
 - ²⁰A. Barbier, R. Belkhou, P. Ohresser, M. Gautier-Soyer, O. Bezencenet, M. Mulazzi, M. J. Guittet, and J. B. Moussy, *Phys. Rev. B* **72**, 245423 (2005).
 - ²¹S. Gota, M. Gautier-Soyer, and M. Sacchi, *Phys. Rev. B* **64**, 224407 (2001).
 - ²²S. Gota, J. B. Moussy, M. Henriot, M. J. Guittet, and M. Gautier-Soyer, *Surf. Sci.* **482-485**, 809 (2001).
 - ²³S. Gota, E. Guiot, M. Henriot, and M. Gautier-Soyer, *Phys. Rev. B* **60**, 14387 (1999).
 - ²⁴A. Barbier, O. Bezencenet, C. Mocuta, J. B. Moussy, H. Magnan, N. Jedrecy, M. J. Guittet, and M. Gautier-Soyer, *Mater. Sci. Eng., B* **144**, 19 (2007).
 - ²⁵R. L. Blake, R. E. Hessevick, T. Zoltai, and L. Finger, *Am. Mineral.* **51**, 123 (1966).
 - ²⁶D. Carbone, O. Plantevin, R. Gago, C. Mocuta, O. Bikondoa, L. Petit, H. Djazouli, A. Alija, and T. H. Metzger, *J. Synchrotron Radiat.* **15**, 414 (2008).
 - ²⁷I. K. Robinson and D. J. Tweet, *Rep. Prog. Phys.* **55**, 599 (1992).
 - ²⁸D. E. Sayers, F. W. Lytle, and E. A. Stern, *Phys. Rev. Lett.* **27**, 1204 (1971).
 - ²⁹H. Magnan, D. Chandesris, B. Villette, O. Heckmann, and J. Lecante, *Phys. Rev. Lett.* **67**, 859 (1991).
 - ³⁰O. Heckmann, H. Magnan, P. Le Fèvre, D. Chandesris, and J. J. Rehr, *Surf. Sci.* **312**, 62 (1994).
 - ³¹A. M. Saib, A. Borgna, J. van de Loosdrecht, P. J. van Berge, and J. W. Niemantsverdriet, *Appl. Catal., A* **312**, 12 (2006).
 - ³²S. A. Chambers, R. F. C. Farrow, S. Maat, M. F. Toney, L. Folks, J. G. Catalano, T. P. Trainor, and G. E. Brown, Jr., *J. Magn. Magn. Mater.* **246**, 124 (2002).
 - ³³O. Bezencenet, A. Barbier, P. Ohresser, R. Belkhou, S. Stanesco, J. Owens, and M. J. Guittet, *Surf. Sci.* **601**, 4321 (2007).
 - ³⁴S. I. Zabinsky, J. J. Rehr, A. Ankudinov, R. C. Albers, and M. J. Eller, *Phys. Rev. B* **52**, 2995 (1995).
 - ³⁵A. Traverse, *New J. Chem.* **22**, 677 (1998).
 - ³⁶M. Rauscher, R. Paniagio, H. Metzger, Z. Kovats, J. Domke, J. Peisl, H. Pfannes, J. Schulze, and I. Eisele, *J. Appl. Phys.* **86**, 6763 (1999).
 - ³⁷R. Lazzari, *J. Appl. Crystallogr.* **35**, 406 (2002).
 - ³⁸A. Barbier, S. Stanesco, C. Boeglin, and J.-P. Deville, *Phys. Rev. B* **68**, 245418 (2003).
 - ³⁹G. Renaud *et al.*, *Science* **300**, 1416 (2003).
 - ⁴⁰J. Mane Mane, C. S. Cojocar, A. Barbier, J.-P. Deville, B. Jean, T. H. Metzger, B. Thiodjio Sendja, and F. Le Normand, *Phys. Status Solidi (RRL)* **1**, 122 (2007).
 - ⁴¹J. Mane Mane, C. S. Cojocar, A. Barbier, J. P. Deville, B. Thiodjio Sendja, and F. Le Normand, *Phys. Status Solidi A* **204**, 4209 (2007).
 - ⁴²L. G. Parratt, *Phys. Rev.* **95**, 359 (1954).
 - ⁴³A. Gibaud and S. Hazra, *Curr. Sci.* **78**, 1467 (2000).
 - ⁴⁴S. Sasaki, KEK, National Laboratory for High Energy Physics Report No. 83-22, 1984 (unpublished).
 - ⁴⁵O. Bezencenet, Ph.D. thesis, Université Paris VI, 2008.